Limits to the Energy-Conversion Efficiency of Air-Bridge Thermophotovoltaics

Jihun Lim[1] and Stephen R. Forrest[1,2,*]

[1]*Department of Electrical Engineering and Computer Science, University of Michigan, Ann Arbor, Michigan 48109, USA*

[2]*Department of Physics and Materials Science and Engineering, University of Michigan, Ann Arbor, Michigan 48109, USA*

Air-bridge thermophotovoltaic (ABTPV) devices demonstrate near-99% utilization of photons whose energy is less than the semiconductor band gap (known as out-of-band, OOB, photons). Here, we determine 55.5% is the thermodynamic limit at an emitter temperature of 1400 K for single junction ABTPVs based on detailed balance, which compares to a thus-far reported efficiency of 32%. A technology computer-aided design model for the (In,Ga)As diode predicts that suppressing the surface-recombination velocity to <200 cm/s significantly improves the open-circuit voltage and the shunt resistance, resulting in 48.6% as the practical efficiency limit. We find that a 1% OOB loss due to free-carrier absorption in doped regions of the TPV can drastically decrease the efficiency at larger band gaps and lower emitter temperature. We also analyze the effects of shadowing by metal grids, which generally introduces only minor losses in TPV performance.

I. INTRODUCTION

Fossil fuels are the primary source of energy consumption in buildings, transportation, and manufacturing [1–3]. However, the usage of these fuels accelerates climate change, deforestation, and scarcity of resources [3–5]. This has attracted increasing interest in non-fossil-fuel sources for the generation of electricity, as exemplified by solar photovoltaic (PV) cells [6–12]. A significant challenge to using renewables, however, is the need for very-low-cost energy storage. Recovery of excess energy stored as heat is one way to eliminate, or augment, commonly used electrochemical or pumped water storage. Specifically, power generation using thermophotovoltaic (TPV) cells has the advantage of employing low-maintenance-cost thermal storage with high power density and without constraints as to their location [13–18].

The basic architecture of a TPV cell is that it has a high efficiency for converting above-band-gap (in band, IB) photons to electrons, while reflecting out-of-band (OOB) low-energy photons back to the source. This design requires a back-surface reflector (BSR) with near-unity reflectivity. The recently introduced air-bridge (AB) TPV provides a unique means to maximize the reuse of OOB photons via loss-free Fresnel reflections [16,19]. Understanding the limits to various approaches to TPV design is necessary to develop guidelines that lead to enhanced energy conversion. In a TPV system design, we must consider three factors: (1) the radiative path between the heat source (the emitter) and the cell; (2) the temperatures of the emitter and the cell; and (3) IB photon absorption efficiency, OOB reflection efficiency, and parasitic photon losses. Among several attempts to more closely approach the TPV thermodynamic efficiency limits, Baldasaro *et al.* stress the importance of parasitic loss of photons and spectral control limitations, which result in a trade-off between the cell band gap and its efficiency [20].

Here, we analyze the efficiency limits of the ABTPV cell based on detailed balance. We employ the Drude model for III-V materials, which quantifies the spectral efficiency (SE) loss due to free-carrier absorption (FCA) in undepleted regions of the cell. We then calculate the efficiency limits of a lattice-matched (In,Ga)As diode, and the SE determined by the active PV membranes suspended between conductive gridlines to form air bridges. We employ a technology computer-aided design (TCAD) model for (In,Ga)As ABTPV cells to include recombination losses that degrade the open-circuit voltage (V_{OC}), shunt-path losses, and the influence of the cell fill factor (FF) and the geometric fill factor (GFF). Finally, we determine the thermodynamic efficiency limits based on a detailed balance and the dependence of OOB photon loss as a function of band gap and emitter temperature.
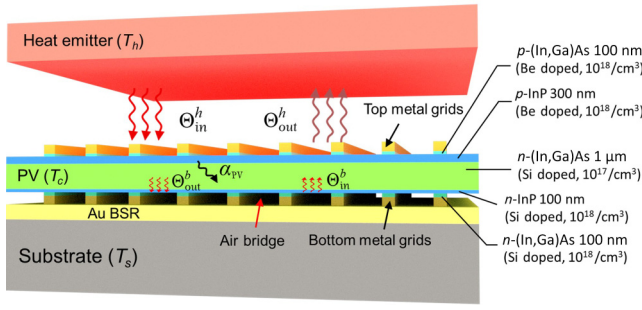
*stevefor@umich.edu

FIG. 1. Schematic illustration of a thermophotovoltaic system composed of a heat emitter, an air-bridge photovoltaic cell with metal grids, and a substrate attached to a heat sink. The PV cell comprises five epilayers of (In,Ga)As and InP.

II. EFFICIENCY LIMITS AND LOSSES IN ABTPVS

Figure 1 illustrates the components of an ABTPV. The PV cell comprises an (In,Ga)As (In : Ga = 0.53:0.47) active region grown by molecular beam epitaxy (MBE) lattice-matched on (100) InP. The transfer of the epitaxy to the Si substrate is achieved via Au-Au cold-weld bonding to the BSR [21]. The top gold metal is deposited by e-beam evaporation, followed by patterning it and the p-type (In,Ga)As contact layer. The blackbody emitter and PV cell are at temperatures of T_h and T_c, respectively, while the substrate temperature (T_s) is also at T_c [19,22]. The paths for photon flux have contributions from the emitter, Θ_{in}^h, and from the BSR, Θ_{in}^b. The flux is reduced by absorption and parasitic loss in the PV cell, expressed by $\Theta_{\text{in}}^h = \alpha_{\text{PV}}^1 + \Theta_{\text{out}}^b$, where α_{PV}^1 comprises the parasitic losses at the metal-semiconductor interface and absorption by the reflector, and Θ_{out}^b is the photon flux reaching the reflector. An air cavity minimizes the losses, thereby leading to $\Theta_{\text{in}}^b \approx \Theta_{\text{out}}^b$ and $\Theta_{\text{in}}^b = \alpha_{\text{PV}}^2 + \Theta_{\text{out}}^h$, where α_{PV}^2 is photon absorption in the PV, giving a total absorption of $\alpha_{\text{PV}} = \alpha_{\text{PV}}^1 + \alpha_{\text{PV}}^2$.

The subband gap, or OOB reflectance, is $R_{\text{OOB}} = \Theta_{\text{in}}^h - \Theta_{\text{out}}^h$. The view factor, VF, is the ratio of overlap of the emitter and detector areas. Since the two blackbodies are planar with areas larger than their separation, VF = 1. The absorption in the PV is the sum of radiative and nonradiative terms, where the nonradiative term is primarily due to defects in the band gap and FCA, which, in turn, decreases SE and the output power of the PV cell (P_{out}). Under illumination, the top and bottom metal gridlines conduct free charges to electrodes at the periphery of the cell. The geometric fill factor, which is the ratio of the metal grid to the total device area, is GFF ≤ 1. This contributes to an additional reduction of SE.

To calculate the maximum achievable energy-conversion efficiency based on detailed balance (i.e., the thermodynamic limit) of ABTPVs for a TPV having unity external quantum efficiency (EQE), we assume that T_c

TABLE I. Parameters used for the ideal and practical (In,Ga)As ABTPV cells.

Parameters	Thermodynamic limit	Practical limit	Practical case [16]
R_{OOB} (%)	100	98.62	97.84
R_s (mΩ cm²)	0	12	26
R_c (Ω cm²)	0	≤2 × 10⁻⁷	2.0 × 10⁻⁵
R_{sh} (Ω cm²)	∞	∞	127.7
v_{surf} (cm/s)	0	0	2 × 10⁵
EQE (%)	100	68	68
IQE (%)	100	100	98

is fixed at 293 K and $R_{\text{OOB}} = 100\%$. Table I compares parameters used to estimate the maximum and practical power-conversion efficiencies (PCEs) of a previously reported (In,Ga)As ABTPV cell [16]. For the practical cell, we include the loss of OOB photons by FCA; series resistance (R_s), including contact resistance (R_c) and junction shunt resistance (R_{sh}); internal quantum efficiency (IQE); and EQE. The practical efficiency limit is calculated by assuming three extrinsic sources: R_{OOB} loss of the cavity mode, less than unity EQE, and ohmic losses. In this approximation, FCA, R_c losses, and Shockley-Reed-Hall (SRH) recombination are neglected. Finally, we consider shadowing by top metal grids, causing additional photon loss.

A. Efficiency limit of a thermophotovoltaic cell

The SE is given by

$$\text{SE} = \frac{E_g \int_{E_g}^{\infty} \varepsilon_{\text{eff}}(E)\Phi(E)dE}{\int_0^{\infty} \varepsilon_{\text{eff}}(E)E\Phi(E)dE}, \quad (1)$$

where $\Phi(E)$ is the photon flux from the emitter and ε_{eff} is the effective emissivity [16,18,23], which is given by [23,24]

$$\varepsilon_{\text{eff}}(E) = \frac{1 - R_e(E)}{1 - R_e(E)R_{\text{cell}}(E)}\alpha_{\text{PV}}. \quad (2)$$

Here, $R_e = 1 - \varepsilon_e$ and R_{cell} are the spectral reflectances of the emitter and the cell, respectively. Next, PCE is given by [20,25]

$$\text{PCE} = \frac{P_{\text{out}}}{P_{\text{abs}}} = \frac{V_{\text{OC}}J_{\text{SC}}\text{FF}}{q\text{VF}\int_0^{\infty} \varepsilon_{\text{eff}}(E)E\Phi(E)dE}$$

$$= \text{SE} \times \text{IQE}\frac{V_{\text{OC}}}{E_g}\text{FF}, \quad (3)$$

where P_{abs} is the TPV-cell absorbed power, and J_{SC} is the short-circuit current. The current-density–voltage characteristics are as follows:

$$J = J_1 \left[\exp\left(\frac{q(V - R_s J)}{k_B T_c} \right) - 1 \right]$$
$$+ J_2 \left[\exp\left(\frac{q(V - R_s J)}{2k_B T_c} \right) - 1 \right] + \frac{V - R_s J}{R_{sh}} - J_{ph},$$
$$(4)$$

where J_1 and J_2 are the saturation current densities for diffusion- and recombination-limited current sources (including bulk and surface recombination), respectively; J_{ph} is the photocurrent density; and k_B is the Boltzmann constant. In the thermodynamic limit, the photocurrent density is given by

$$J_{ph} = q\text{VF} \int_0^{\lambda_g} \frac{\varepsilon_e(\lambda)}{1 - R_e(\lambda)R_{cell}(\lambda)} \text{IQE}(\lambda)\alpha_{cell}(\lambda)\Phi(\lambda)d\lambda.$$
$$(5)$$

Here, $J_{ph} = J_{SC}$ and IQE = 100%. From Eq. (4), V_{OC} is expressed by

$$V_{OC}^{rad} = \frac{k_B T_c}{q} \ln\left(\frac{J_{SC} - (V_{OC}/R_{sh})}{J_1 + J_2 \exp(-(qV_{OC}/2k_B T_c))} \right)$$
$$\cong \frac{k_B T_c}{q} \ln\left(\frac{J_{SC} - (V_{OC}/R_{sh})}{J_1} \right),$$
$$(6)$$

Including nonradiative (NR) recombination, the voltage is decreased by

$$\Delta V_{loss} = V_{OC}^{rad} - V_{OC}^{NR}$$
$$= \frac{k_B T_c}{q} \ln\left(\frac{J_{SC}^{rad}}{J_{SC}^{NR} - (V_{OC}^{NR}/R_{sh})} \frac{J_1^{NR}}{J_1^{rad}} \right).$$
$$(7)$$

The origin of ΔV_{loss} in the AB device is understood using the diode-current equation:

$$J_D = J_{SC} + q\frac{Dn_i^2}{N_d W_d}[\exp(qV/k_b T_c) - 1]\Big|_{rad}$$
$$+ \frac{qn_i W_d}{\tau_{SRH}}(\exp(qV/2k_B T_c) - 1)\Big|_{NR},$$
$$(8)$$

where $N_d = 10^{17}/\text{cm}^3$ is the carrier concentration in the (In,Ga)As active layer, W_d is the depletion width at the p-n junction, D is the diffusion coefficient of minority-carrier holes, n_i is the intrinsic carrier concentration, and τ_{SRH} is the SRH recombination time [26]. Equation (8) is identical to Eq. (4), where $V \to V - R_s J_D$, and implies the importance of the depletion width, affecting both the radiative and nonradiative terms. V_{OC} at $J_D = 0$ is determined by

N_d, which varies with W_d and τ_{SRH}. The recombination lifetime (τ_c) is given by

$$\frac{1}{\tau_c} \cong \frac{1}{\tau_{SRH}} + \frac{1}{\tau_{rad}} \cong (\tau_{SRH}^{-1} + BN_d),$$
$$(9)$$

where B is the radiative-recombination coefficient:

$$B_{rad} = \frac{2\pi}{n_i^2 h^3 c^2} \int_{E_g}^{\infty} E^2 \alpha(E)\exp^{(-(E/k_B T))} dE,$$
$$(10)$$

where n_i is the intrinsic carrier concentration, c is the velocity of light, and $\alpha = 4\pi k_r/\lambda$ [27]. We obtain $B_{rad} = 2.0 \times 10^{-10}$ cm^3 s^{-1} [28,29] and $\tau_c = 30$ ns [30, 31] using TCAD. This matches other reports (17–70 ns) on (In,Ga)As [28,32]. The practical limit assumes that $\tau_{SRH} \to \infty$ and $B_{rad} = 4.1 \times 10^{-12}$ cm^3 s^{-1}. Rewriting Eq. (6), J_{SC} is expressed by

$$J_{SC} \approx \exp(qV_{OC}/k_B T_c)\left[q\frac{Dn_i^2}{N_d W_d} + \frac{qn_i W_d}{\tau_{SRH}}(e^{-qV_{OC}/2k_B T_c}) \right],$$
$$(11)$$

where the first term in square brackets is about 10^{-8} A/cm^2. At $\tau_{SRH} > 1$ μs, the second term is $<10^{-10}$ A/cm^2, and hence, is negligible.

Finally, the open-circuit voltage of the (In,Ga)As TPV in the thermodynamic limit is $V_{OC} = 0.63$ V ($T_c = 293$ K, $T_h = 1450$ K, $E_g = 0.74$ eV) given by [20,33,34]

$$V_{OC}^{rad} = k_B T_c \ln\left(\frac{J_{SC}}{J_0} + 1 \right)\Big|_{rad}$$
$$= E_g \left(1 - \frac{T_c}{T_h} + \frac{k_B T_c}{E_g} \ln\left(\frac{T_h}{T_c} \right) \right).$$
$$(12)$$

As R_{sh} decreases, ΔV_{loss} increases from Eq. (7) [22].

Figure 2(a) shows the thermodynamic limited J-V characteristics (blue circles) corresponding to $R_{sh} \to \infty$ and $R_s \to 0$. Also shown is the measured dark current from the ABTPV in Ref. [16], along with a fit to Eq. (4) (red solid line), yielding $R_{sh} = 1$ MΩ cm^2, $R_c = 2.02 \times 10^{-5}$ Ω cm^2, and $R_s = 26$ mΩ cm^2. The gray-filled symbols show the practical limit where the SRH recombination is negligible, resulting in $R_s = 12$ mΩ cm^2 and $R_c \to 0$, whereas, at the thermodynamic limit, we have $R_s = 0$ and $R_{sh} = \infty$.

From Eq. (5), the J_{SC} is calculated for a blackbody spectrum of 1500 K as a function of VF, as shown in Fig. 2(b), which agrees with experimental results (filled circles), suggesting that the IQE approaches 100% [16,25]. The ABTPV in Ref. [1] has EQE = 68%, which is limited by the Fabry-Perot cavity oscillations and the TPV thickness [35]. For EQE = 100%, J_{SC} is increased by 62% compared to the solid line. The (In,Ga)As ABTPV shows $\Delta V_{loss} = 0.15$ V with $R_{sh} = 200$ Ω cm^2 under $T_h = 1470$ K [36], as shown in Fig. 2(c).
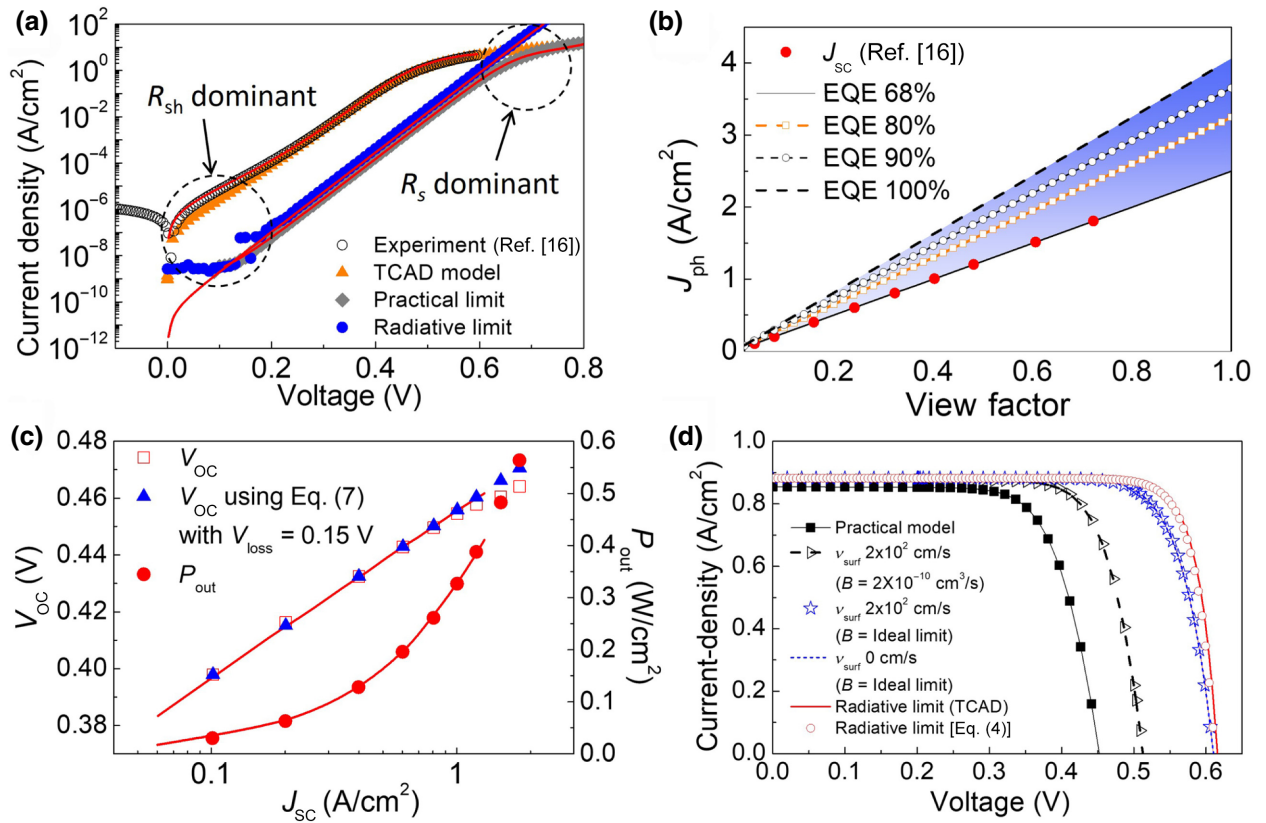
FIG. 2. (a) Dark current-density–voltage (J-V) characteristics of an (In,Ga)As/InP ABTPV cell. The low-bias region (<0.1 V) is governed by the junction shunt resistance (R_{sh}), and the high-bias region (>0.4 V) is dominated by series resistance (R_s). Open circles are for the (In,Ga)As ABTPV cell from Ref. [16]; triangles are from the TCAD model; diamonds show the practical limits of the (In,Ga)As ABTPVs, where contact resistance (R_c), R_{sh}, and SRH recombination are negligible; and filled circles are for the thermodynamic (radiative) limit ($R_s = 0$, $R_{sh} = \infty$). Solid curves are fits using Eq. (4). (b) Photocurrent density (J_{ph}) calculated as a function of VF. Solid dots are from the device in Ref. [16]. Yellow, white, and black dashed lines assume EQE of 80%, 90%, and 100%, respectively. (c) Open-circuit voltage (V_{OC}) and electrical output power (P_{out}) as functions of the short-circuit current density (J_{SC}) calculated using a TCAD method for the air-bridge (In,Ga)As TPV [16]. Filled triangles are the calculated V_{OC}, assuming $V_{loss} = 0.15$ V using Eq. (7). (d) J-V characteristics for the (In,Ga)As ABTPV cell simulated using TCAD. Black squares follow the model fit to Ref. [16]. Remaining curves are simulated for various surface-recombination velocities (v_{surf}) and radiative-recombination coefficients (B) noted in the legend. Blue solid line indicates the limiting performance with $v_{surf} = 0$ cm/s and $B = 4.09 \times 10^{-12}$ cm^3/s. Red solid line and circles are the thermodynamic limits simulated using Eq. (4) and TCAD modeling.

Figure 2(d) compares the different fourth-quadrant J-V characteristics for $T_h = 1500$ K at the thermodynamic limit compared with those of the practical (In,Ga)As ABTPV. The model ignores nonradiative recombination [36]. However, P_{out} increases by more than 53% compared to the model based on measured ABTPV performance for a surface-recombination velocity of $v_{surf} = 200$ cm/s and $B = B_{rad}$. The red circles represent the thermodynamic limit calculated using Eq. (4), and the TCAD solution in which the limit to the dark current density is calculated by integrating the blackbody spectrum ($T_c = 293$ K) over the in-band region [20]. P_{out} increases by only 7% compared to the blue stars, implying that shunt currents strongly affect diode performance. The J_{SC} difference is only 3% between the ideal and the practical cases.

B. Spectral efficiency loss from free-carrier absorption

At infrared wavelengths, the interaction of free carriers with infrared photons results in a decreased R_{OOB}. The Drude model is used to calculate the extinction coefficient [37,38]:

$$k_r = \frac{1}{4\pi} (\lambda^\gamma C n), \quad (13)$$

where λ is the wavelength, γ and C are parameters dependent on the sample reflectance, and n is the free-carrier concentration. The parameters for (In,Ga)As and InP are listed in Table II. The theory is based on the scattering time of a free charge, which, in turn, depends on the carrier concentration, charge mobility, and temperature

TABLE II.   Drude model parameters for (In,Ga)As and InP.

Material	γ	C
(In,Ga)As	3.04	3.33×10^{-18}
InP	3.13	3.71×10^{-18}

(see S2 within the Supplemental Material for the Drude theory [49]) [38]. For our study, therefore, γ is empirically determined. The dashed and dotted lines in Fig. 3(a) indicate the Fourier-transform infrared spectroscopic measurements for a Au BSR (In,Ga)As TPV cell. The solid line and shaded area are from simulations using the transfer-matrix method (TMM). In the absence of FCA, the k_r at sub-band-gap energies of <0.74 eV is zero, and k_r is calculated to fit the measured Fourier-transform infrared spectroscopy (FTIR) results using Eq. (13) in the presence of FCA. From simulations, $R_{OOB}=94.4\%$ at photon energies of $E_{ph}=0.12$–0.74 eV, without FCA, and 91.3% when it is included, giving an excess loss of $\Delta R_{OOB}=3.1\%$. A large portion of the loss is due to the undepleted layers (with $n > 10^{18}$/cm^3). The Fabry-Perot oscillations are determined by the total PV thickness.

Figure 3(b) shows the relationship between SE and R_{OOB} for the TPV in Fig. 1, assuming an effective emitter emissivity of unity. The trend reveals that a relatively high R_{OOB} leads to higher efficiency, although the improvement decreases with T_h.

C. Losses due to out-of-band photon mirroring by the air-bridge reflector

Figure 4(a) shows the calculated absorption spectrum of the (In,Ga)As ABTPV structure with an air gap of 0.6 μm [16]. Once more neglecting FCA, we find $R_{OOB}=98.6\%$ for $\lambda = 1.68$–15 μm. The additional loss of $\Delta R_{OOB}=1.4\%$ is due to modal oscillations in the air

cavity. $R_{OOB}=97.8\%$ (corresponding to $\Delta R_{OOB}=0.8\%$) when FCA is included (FCA-1). When FCA is negligible, R_{OOB} is reduced to 98.1% ($\Delta R_{OOB}=0.5\%$) (FCA-2). In this case, the reduction is largely due to the relatively-highly-doped InP layers. Figure 4(b) compares R_{OOB} for AB and Au-BSR TPVs using the same diode structure. R_{OOB} is weighted by the blackbody emission spectrum as a function of temperature following $R_{OOB} = \int_0^{E_g} (1 - A_c) H(E, T_h) dE / \int_0^{E_g} H(E, T_h) dE$, where A_c is the cell absorption and H is the spectral power density of a blackbody. The shaded region indicates the improvement in reflectivity achieved by replacing the Au BSR with an air bridge, resulting in a significant increase in R_{OOB} by 2.5% to 3.7%. The dashed regions are the loss, ΔR_{OOB}, due to FCA, which is about 1% at $T_h > 1300$ K for the ABTPV. In Fig. 4(c), we observe that the relationship between SE and R_{OOB} becomes important at a relatively low T_h, where the difference in SE between the AB and Au BSR devices is 23% at $T_h = 900$ K, but it is reduced to less than 3% at $T_h > 1700$ K. Figure 4(d) shows the dependence of PCE on SE as a function of T_h and R_{OOB}, where the diode is assumed to exhibit only radiative recombination of charge carriers. Compared to the Au BSR, the ABTPV cell leads to $>40\%$ increase in efficiency for $T_h > 900$ K. For $R_{OOB}=1$, PCE exceeds 40%, even at the lowest temperatures.

D. Loss due to the geometric fill factor

The current density in TPVs is typically much higher than in solar PVs due to the proximity of the thermal source. For this reason, it is important to use conductive gridlines to extract the photocurrent with minimum resistance loss. Hence, there is a trade-off in efficiency between gridline shadowing and series resistance. The area occupied by the gridlines is the geometric fill factor, GFF =
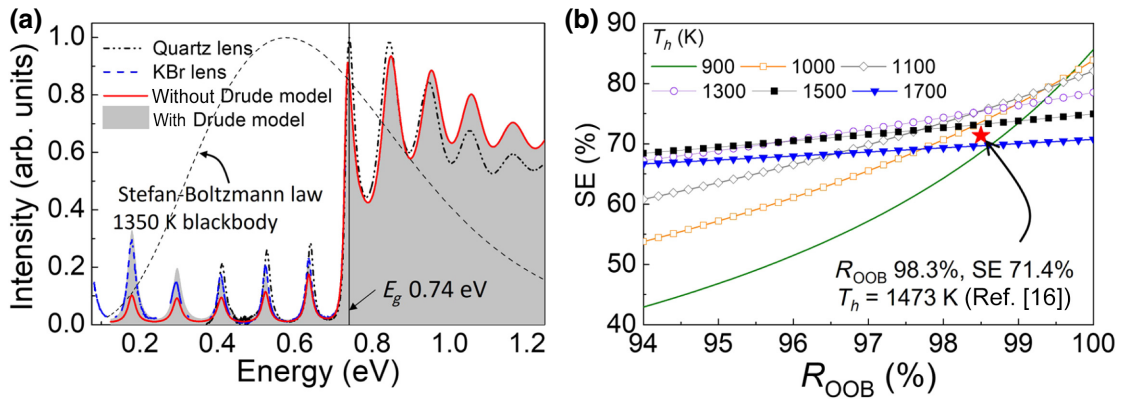

FIG. 3.   (a) Measured and simulated FTIR spectrum for Au BSR (In,Ga)As TPV. FTIR measurements are performed using two different lenses [quartz ($\lambda = 1.0$–3.57 μm) and KBr (1.70–15.4 μm)]. Drude-model simulation fits the measured spectrum. (b) Calculation of spectral efficiency as a function of R_{OOB} for several emitter temperatures, T_h.
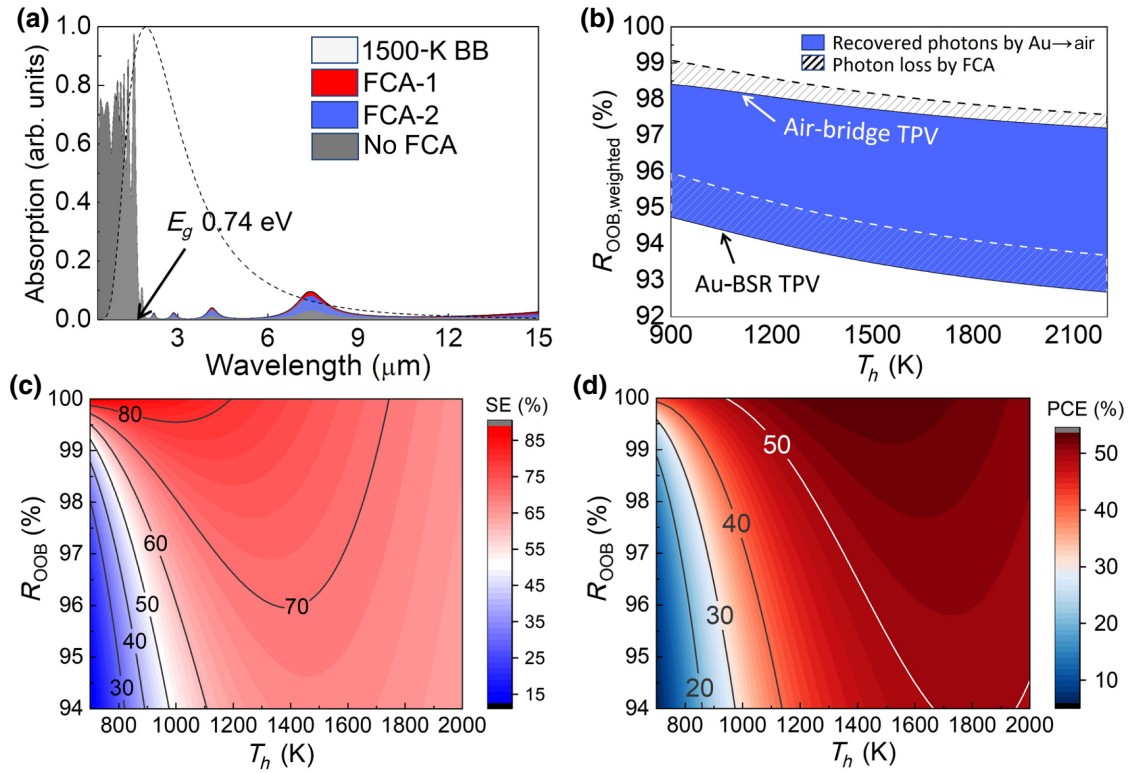
FIG. 4. (a) Simulated power-distribution spectrum for the (In,Ga)As air-bridge TPV in Fig. 1. FCA-1 corresponds to doped (In,Ga)As and InP, whereas FCA-2 assumes doping only in InP. Dotted line is the 1500-K blackbody (BB) spectrum. (b) Calculated R_{OOB} versus T_h. Cross-hatched region is the loss due to FCA, and shaded region is due to improvements in R_{OOB} achieved by replacing the Au BSR with air. (c) Contour plot of SE as a function of R_{OOB} and T_h. With decreasing R_{OOB}, SE significantly drops at a relatively low T_h (left bottom), implying that the importance of a high R_{OOB} increases at a low T_h. (d) Contour plot of the maximum PCE as a function of R_{OOB} and T_h. As R_{OOB} increases, variation of the PCE becomes less sensitive to T_h.

$[(W_{PV} - W_M)W_{PV}]/(W_{PV})^2$, assuming a square cell configuration, where W_{PV} is the open cell width, and W_M is the area occupied by the gridlines [see Fig. 5(a)]. The metal grid reduces the SE as follows [cf. Eq. (1)]:

$$ SE = \frac{GFF E_g \int_{E_g}^{\infty} \varepsilon_{eff}(E) \Phi(E) dE \Big|_{PV}}{GFF \int_0^{\infty} \varepsilon_{eff,PV}(E) E \Phi(E) dE \Big|_{PV} + (1 - GFF) \int_0^{\infty} \varepsilon_{eff,M}(E) E \Phi(E) dE \Big|_{metal}}, \quad (14) $$

where $\varepsilon_{eff,PV}$ and $\varepsilon_{eff,M}$ are the effective emissivities of the active area and metal grid, respectively. The numerator is the absorption in the PV region, and the denominator expresses the total reflected photons from the BSR and the gridlines.

Since $\varepsilon_{eff,M} < 1$, there are losses from light reflected from the metal surface. Figures 5(b) and 5(c) show the SE and cell efficiencies for 1%, 5%, and 10% reflectance losses by the gridlines, and GFF = 83% for the (In,Ga)As ABTPV cell in Ref. [16]. The reflectance loss can be higher than 10%, depending on the materials and

gridline structures. The edge of the shaded region shows the limit of the (In,Ga)As ABTPV in Ref. [16]. The reflectance loss is particularly significant at low T_h. Figure 5(d) illustrates the trade-off between cell resistance and GFF using the TCAD-simulated FF, P_{out}, and PCE. The dashed line is the calculated PCE at $T_h = 1500$ K, corresponding to the upper limit of the SE in Fig. 5(b). The triangle and circle symbols are the PCE using the SE limited by reflectance losses by the gridlines of 1% and 10%, respectively. While an optimal P_{out} is found at GFF between 0.82 and 0.85, an optimized PCE is found at a
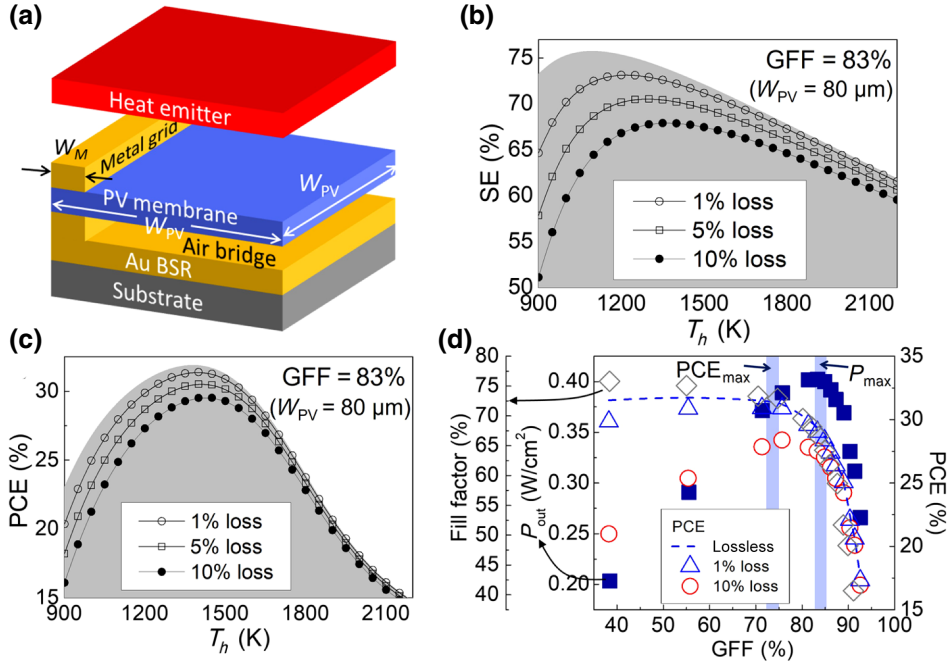
FIG. 5. (a) Device geometry used to calculate the GFF. W_M is the metal-grid width, and W_{PV} is the width and length of the device. (b) Spectral efficiency of the air-bridge (In,Ga)As TPV calculated as a function of emitter temperature for $W_{PV} = 80$ μm and $W_M = 8$ μm. Shaded region indicates the SE limit for the (In,Ga)As ABTPV structure in Ref. [16]. (c) PCE versus T_h. Shaded region assumes perfect reflectivity of the metal-grid lines. (d) Left axis, FF (diamonds) and P_{out} (squares) using TCAD to model the (In,Ga)As ABTPV cell. Right axis, calculated PCE assuming $R_{loss} = 1\%$ (triangles) and 10% (circles). Dashed line is the practical efficiency limit assuming GFF = 100%.

relatively smaller GFF to maximize $PCE_{TPV} = IQE V_{OC} FF$ [see Eq. (3)]. In the TCAD simulations, we change the GFF by varying only the spacing between gridlines.

III. DISCUSSION

Figure 6(a) shows the PCE versus T_h, including the effects of different loss mechanisms discussed in Sec. II. The upper boundary shows the thermodynamic limit of the single junction (In,Ga)As ABTPV efficiency with $R_{OOB} = 100\%$ and EQE = 100%, where maximum PCE = 57.2%. The practical (In,Ga)As ABTPV structure has maximum EQE = 68%, resulting in the second boundary line with $R_{OOB} = 100\%$ and IQE = 100%. The absorption oscillations in the OOB [see Fig. 4(a)] introduce "cavity loss." The dotted line indicates the boundary at $R_s = 0$, such that the yellow region indicates the ohmic losses. The practical limit of the (In,Ga)As cell assumes negligible R_c and SRH, and $R_s = 12$ mΩ cm², leading to maximum PCE = 48.6%. The upper boundary of the orange region is the maximum PCE in the absence of nonradiative recombination, the suppression of which is clearly critical to achieving high efficiency. The bottom solid line is for the (In,Ga)As ABTPV, where the red dashed line indicates the (In,Ga)As model with VF = 0.3, corresponding to the conditions used for the device indicated by the star [16]. The violet-colored region is the loss due to a contact resistance

of $R_c = 2 \times 10^{-5}$ Ω cm², with the loss becoming negligible for $R_c \leq 2 \times 10^{-7}$ Ω cm². Among the different losses, recombination is the largest contributor. At a relatively high temperature, the ohmic loss due to metal grids and R_c causes another large loss. In a practical TPV system, the photon-recycling efficiency depends on the effective emissivity, ε_{eff}, determined by the emitter and detector materials and reflectivities [see Eq. (2)]. This can produce additional loss that is not considered in Fig. 6(a), where we assume $\varepsilon_{eff} = 1$ for both the detector and emitter.

Figure 6(b) shows the PCE limit (EQE = 1% and $R_{OOB} = 100\%$) as a function of E_g and T_h. The dashed line addresses the maximum PCE versus the normalized band gap, E_g/kT, where the corresponding T_h decreases with band gap. Figure 6(c) shows the dependence of the maximum PCE versus E_g/kT_h for various R_{OOB}. A R_{OOB} decrease from 100% to 96% results in a reduced PCE for an increasing band gap. Larger band gaps ($E_g > 1.0$ eV) are useful at high emitter temperatures (1900–2400 °C) commonly found in low-cost thermal-energy grid storage [39,40]. Recently, however, the efficient conversion of low-temperature heat to electricity has also become important [41]. The symbols in Fig. 6(c) represent published PCE results [16,19,25,39,42–48]. The air-bridge TPV cell (red star) apparently achieves the highest efficiency among single-junction TPVs. The large gap between current
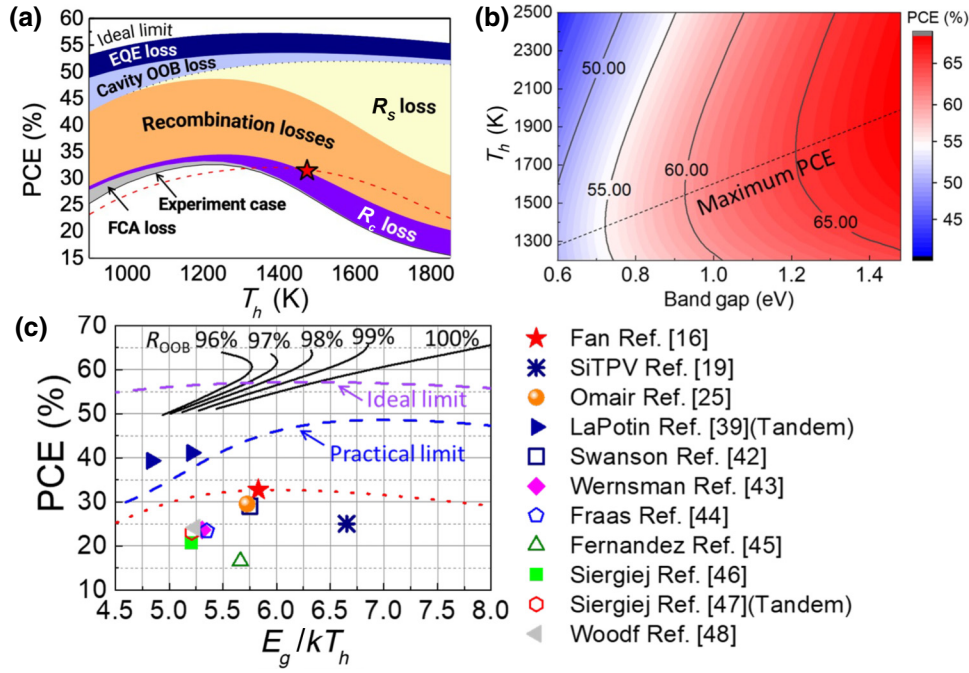
FIG. 6. (a) Calculation of the air-bridge PCE limits with the relative effects of various losses. Maximum PCE limit corresponds to EQE = 100% and R_{OOB} = 100%. Cavity OOB loss is calculated using R_{OOB}, ignoring FCA in Fig. 4(a). The practical limit corresponds to the case where the contact resistance (R_c) and bulk recombination are negligible. The orange region includes loss from surface recombination. The violet-shaded region is the power loss due to the device contact resistance, and the gray-shaded region is due to FCA loss. The bottom solid line indicates expectations for practical ABTPVs. The dashed line is the model for the device in Ref. [1], where VF = 0.3. Red star is the maximum PCE achieved for the (In,Ga)As ABTPV in Ref. [1]. (b) Contour plot of the PCE at R_{OOB} = 100% with the thermodynamic limit as a function of band gap and emitter temperature. The dashed line is the maximum PCE, showing that the normalized band gap (E_g/kT_h) increases with E_g. (c) PCE as a function of E_g/kT_h for previous results (symbols) reported in the literature. Solid lines are the calculated maximum PCE at R_{OOB} = 100% with the thermodynamic limit with various R_{OOB}. The band gap (E_g) is varied from 0.6 to 1.4 eV. Dashed lines indicate the calculated ideal PCE and practical limits for the (In,Ga)As ABTPV cell [16].

device performance and the thermodynamic limit suggests the possibility of achieving considerably higher single-junction ABTPV efficiencies, particularly if recombination is reduced.

IV. CONCLUSIONS

We analyze the performance of the (In,Ga)As ABTPV cell by identifying various losses, including FCA, non-radiative, and ohmic losses, and metal-grid shadowing. The free carriers in relatively-highly-doped semiconductors primarily lead to the loss of R_{OOB}. With $\Delta R_{OOB} = 2\%$, large-band-gap semiconductors (e.g., Si and GaAs) become highly inefficient at low T_h. The largest PCE loss results from recombination at the semiconductor surface. The (In,Ga)As diode model indicates that $v_{surf} < 2 \times 10^5$ cm/s leads to a voltage loss of 0.15 V and approaches zero at $v_{surf} \leq 200$ cm/s. This results in efficiency improvement of 12%–17% at $T_h = 900$–2000 K. At $T_h = 1400$ K, the maximum efficiency at the thermodynamic limit of an (In,Ga)As ABTPV is 55.5%. Trade-offs between cell resistance and shadowing by the metal grid leads to an optimal (In,Ga)As ABTPV P_{out} for GFF = 84%. In conclusion, the voltage loss by recombination results in a significant fraction of efficiency loss compared to the practical PCE limit, implying that the device surface must be improved to reach even higher efficiencies than the highest-performing single-junction ABTPV cells reported to date. This can be achieved by high-purity epitaxial growth (e.g., via metal-organic CVD vs MBE) to reduce recombination in the depletion region, and the suppression of junction shunt paths at the insulator-semiconductor interface.

APPENDIX: TCAD SIMULATION

The air-bridge (In,Ga)As TPV simulations are performed using Synopsys Sentaurus (Version S-2021.06), which simulates the charge-carrier distribution and transport by solving the charge continuity, Poisson, and drift-diffusion equations. In the simulator (Sentaurus Device), the SRH model is included to account for nonradiative recombination. Also, the TMM solver calculates light propagation under the blackbody spectrum. The Drude model reflects the FCA effect during light propagation. We use the Sentaurus default material database (DB) for $In_{0.53}Ga_{0.47}As$, InP, and metals. In the DB, the physics parameters of $In_xGa_{1-x}As$ follow the linear interpolation method using corner materials (InAs, GaAs). In the DB, the material air is not built-in, and therefore, its material properties are added manually. Parameters for air: permittivity constant $(\varepsilon) = 1$, refractive index $= 1$, complex refractive index $(n_r$ and $k_r) = 1$ and 0, resistivity $(\Omega \, cm) = 10^{13}$. The whole set of J-V fitting curves are given in Fig. S1 within the Supplemental Material [49]. Figure S2 within the Supplemental Material [49] shows the J-V curves used for Fig. 5(d). The GFF is varied from 0.38 to 0.93.

[1] S. Mekhilef, R. Saidur, and A. Safari, A review on solar energy use in industries, Renewable Sustainable Energy Rev. **15**, 1777 (2011).

[2] S. Kusch-Brandt, Urban renewable energy on the upswing: A spotlight on renewable energy in cities in REN21's "Renewables 2019 Global Status Report", Resources-Basel **8**, 139 (2019).

[3] F. Martins, C. Felgueiras, M. Smitkova, and N. Caetano, Analysis of fossil fuel energy consumption and environmental impacts in European countries, Energies **12**, 964 (2019).

[4] W. R. Cline, *The economics of global warming* (Institute for International Economics, Washington, 1992), pp. xi, 399 p.

[5] W. Nordhaus, Evolution of modeling of the economics of global warming: Changes in the DICE model, 1992–2017, Climatic Change **148**, 623 (2018).

[6] D. Carson and C. Wronski, Amorphous silicon solar-cell, Appl. Phys. Lett. **28**, 671 (1976).

[7] R. Knechtli, R. Loo, and G. Kamath, High-efficiency GaAs solar-cells, IEEE Trans. Electron Devices **31**, 577 (1984).

[8] M. Green, E. Dunlop, J. Hohl-Ebinger, M. Yoshita, N. Kopidakis, and X. Hao, Solar cell efficiency tables (version 57), Prog. Photovoltaics **29**, 3 (2021).

[9] M. Hermle, F. Feldmann, M. Bivour, J. Goldschmidt, and S. Glunz, Passivating contacts and tandem concepts: Approaches for the highest silicon-based solar cell efficiencies, Appl. Phys. Rev. **7**, 021305 (2020).

[10] K. Lee, J. Zimmerman, T. Hughes, and S. Forrest, Non-destructive wafer recycling for low-cost thin-film flexible optoelectronics, Adv. Funct. Mater. **24**, 4284 (2014).

[11] J. You, L. Dou, K. Yoshimura, T. Kato, K. Ohya, T. Moriarty, K. Emery, C. Chen, J. Gao, G. Li, and Y. Yang, A polymer tandem solar cell with 10.6% power conversion efficiency, Nat. Commun. **4**, 1446 (2013).

[12] F. Yang, M. Shtein, and S. Forrest, Controlled growth of a molecular bulk heterojunction photovoltaic cell, Nat. Mater. **4**, 37 (2005).

[13] D. L. Chubb, *Fundamentals of thermophotovoltaic energy conversion* (Elsevier, Amsterdam, Netherlands; Boston; Oxford, UK, 2007), p. 1 online resource (531p.).

[14] T. Coutts, A review of progress in thermophotovoltaic generation of electricity, Renewable Sustainable Energy Rev. **3**, 77 (1999).

[15] A. Lenert, D. Bierman, Y. Nam, W. Chan, I. Celanovic, M. Soljacic, and E. Wang, A nanophotonic solar thermophotovoltaic device, Nat. Nanotechnol. **9**, 126 (2014).

[16] D. Fan, T. Burger, S. McSherry, B. Lee, A. Lenert, and S. Forrest, Near-perfect photon utilization in an air-bridge thermophotovoltaic cell, Nature **586**, 237 (2020).

[17] A. Fiorino, L. Zhu, D. Thompson, R. Mittapally, P. Reddy, and E. Meyhofer, Nanogap near-field thermophotovoltaics, Nat. Nanotechnol. **13**, 806 (2018).

[18] T. Burger, C. Sempere, B. Roy-Layinde, and A. Lenert, Present efficiencies and future opportunities in thermophotovoltaics, Joule **4**, 1660 (2020).

[19] B. Lee, R. Lentz, T. Burger, B. Roy-Layinde, J. Lim, R. Zhu, D. Fan, A. Lenert, and S. Forrest, Air-bridge Si thermophotovoltaic cell with high photon utilization, ACS Energy Lett. **7**, 2388 (2022).

[20] P. Baldasaro, J. Raynolds, G. Charache, D. DePoy, C. Ballinger, T. Donovan, and J. Borrego, Thermodynamic analysis of thermophotovoltaic efficiency and power density tradeoffs, J. Appl. Phys. **89**, 3319 (2001).

[21] J. Lim, D. Fan, B. Lee, and S. Forrest, Understanding and Control of Compressively Buckled Semiconductor Thin Films, Phys. Rev. Appl. **16**, 064010 (2021).

[22] B. Roy-Layinde, T. Burger, D. Fan, B. Lee, S. McSherry, S. Forrest, and A. Lenert, Sustaining efficiency at elevated power densities in InGaAs airbridge thermophotovoltaic cell, Sol. Energy Mater. Sol. Cells **236**, 111523 (2022).

[23] R. Mahorter, B. Wernsman, R. Thomas, and R. Siergiej, Thermophotovoltaic system testing, Semicond. Sci. Technol. **18**, S232 (2003).

[24] A. Motmaen, A. Rostami, and S. Matloub, Ultra high-efficiency integrated mid infrared to visible up-conversion system, Sci. Rep. **10**, 9325 (2020).

[25] Z. Omair, G. Scranton, L. Pazos-Outon, T. Xiao, M. Steiner, V. Ganapati, P. Peterson, J. Holzrichter, H. Atwater, and E. Yablonovitch, Ultraefficient thermophotovoltaic power conversion by band-edge spectral filtering, Proc. Natl. Acad. Sci. U. S. A. **116**, 15356 (2019).

[26] Y. Zhao and S. He, The experimental investigation on dark current for InGaAs-InP avalanche photodiodes, Microelectron. Eng. **98,** 19 (2012).

[27] A. Kirk, *Solar photovoltaic cells: Photons to electricity* (Academic Press, London, [England], 2015), p. 1 online resource (138p.).

[28] R. K. Ahrenkiel, R. Ellingson, S. Johnston, and M. Wanlass, Recombination lifetime of $In_{0.53}Ga_{0.47}As$ as a function of doping density, Appl. Phys. Lett. **72,** 3470 (1998).

[29] W. Metzger, M. Wanlass, R. Ellingson, R. Ahrenkiel, and J. Carapella, Auger recombination in low-band-gap *n*-type InGaAs, Appl. Phys. Lett. **79,** 3272 (2001).

[30] D. L. Scharfetter and H. K. Gummel, Large-signal analysis of a silicon read diode oscillator, IEEE Trans. Electron Devices **ED16,** 64 (1969).

[31] J. G. Fossum and D. S. Lee, A physical model for the dependence of carrier lifetime on doping density in nondegenerate silicon, Solid-State Electron. **25,** 741 (1982).

[32] T. Asar, S. Ozcelik, and E. Ozbay, Structural and electrical characterizations of $In_xGa_{1-x}As$/InP structures for infrared photodetector applications, J. Appl. Phys. **115,** 104502 (2014).

[33] C. H. Henry, Limiting efficiencies of ideal single and multiple energy-gap terrestrial solar-cells, J. Appl. Phys. **51,** 4494 (1980).

[34] U. Rau, U. Paetzold, and T. Kirchartz, Thermodynamics of light management in photovoltaic devices, Phys. Rev. B **90,** 035211 (2014).

[35] G. Quinchard, T. Poletti, R. Zakhama, J. Pereira, A. Larrue, G. Badano, C. Licitra, R. de Lamaestre, J. Reverchon, and A. Delga, Revisiting the Fabry-Perot reflectivity method for mid-infrared optical index measurement: Case study of InGaAs, AlInAs, and InP, Appl. Opt. **61,** 4079 (2022).

[36] E. Moon, D. Blaauw, and J. Phillips, Infrared energy harvesting in millimeter-scale GaAs photovoltaics, IEEE Trans. Electron Devices **64,** 4554 (2017).

[37] I. T. Sorokina and K. L. Vodopyanov, *Solid-State Mid-Infrared Laser Sources* (Springer Berlin Heidelberg, Imprint: Springer, Berlin, Heidelberg, 2003), vol. online resource (XVI), p. 561 online resource (XVI).

[38] S. Baker-Finch, K. McIntosh, D. Yan, K. Fong, and T. Kho, Near-infrared free carrier absorption in heavily doped silicon, J. Appl. Phys. **116,** 063106 (2014).

[39] A. LaPotin, K. Schulte, M. Steiner, K. Buznitsky, C. Kelsall, D. Friedman, E. Tervo, R. France, M. Young, A. Rohskopf, *et al.*, Thermophotovoltaic efficiency of 40%, Nature **604,** 287 (2022).

[40] C. Amy, H. Seyf, M. Steiner, D. Friedman, and A. Henry, Thermal energy grid storage using multi-junction photovoltaics, Energy Environ. Sci. **12,** 334 (2019).

[41] M. Ishikawa, M. Terauchi, T. Komori, and J. Yasuraoka, Development of high efficiency gas turbine combined cycle power plant, Tech. Rev. - Mitsubishi Heavy Ind. **45,** 15 (2008).

[42] R. M. Swanson, in *International Electron Devices Meeting* (IEEE, 1980), pp. 186–189.

[43] B. Wernsman, R. Siergiej, S. Link, R. Mahorter, M. Palmisiano, R. Wehrer, R. Schultz, G. Schmuck, R. Messham, S. Murray, *et al.*, Greater than 20% radiant heat conversion efficiency of a thermophotovoltaic radiator/module system using reflective spectral control, IEEE Trans. Electron Devices **51,** 512 (2004).

[44] L. Fraas, J. Samaras, H. Huang, L. Minkin, J. Avery, W. Daniels, and S. Hui, in *Proceedings of 17th European PV Solar Energy Conference, Munich, Germany* (2001), Vol. 26.

[45] J. Fernandez, F. Dimroth, E. Oliva, M. Hermle, A. Bett, C. Algora, and C. V, *AIP Conference Proceedings* (Thermophotovoltaic Generation of Electricity, 2007), Vol. 890, p. 190.

[46] R. R. Siergiej, S. Sinharoy, T. Valko, R. J. Wehrer, B. Wernsman, S. D. Link, R. W. Schultz, and R. L. Messham, *AIP Conference Proceedings* (American Institute of Physics, 2004), Vol. 738, p. 480.

[47] R. Siergiej, B. Wernsman, S. Derry, R. Mahorter, R. Wehrer, S. Link, M. Palmisiano, R. Messham, S. Murray, and C. Murray, *AIP Conference Proceedings* (American Institute of Physics, 2003), Vol. 653, p. 414.

[48] D. Woolf, E. Kadlec, D. Bethke, A. Grine, J. Nogan, J. Cederberg, D. Burckel, T. Luk, E. Shaner, and J. Hensley, High-efficiency thermophotovoltaic energy conversion enabled by a metamaterial selective emitter, Optica **5,** 213 (2018).

[49] See the Supplemental Material at http://link.aps.org/supplemental/10.1103/PhysRevApplied.19.034099 for numerical methods used in TCAD and FCA calculations.

[50] W. Bolton, *Control systems* (Newnes, Oxford, UK, 2002).

[51] J. Lim, B. Oh, W. Lee, K. Lee, H. Na, B. Kim, D. Seo, J. Han, and J. Hwang, Selective liquid crystal molecule orientation on ion beam irradiated tantalum oxide ultrathin films, Appl. Phys. Lett. **95,** 123503 (2009).

[52] G. Branch and T. Mihran, Plasma frequency reduction factors in electron beams, IRE Trans. Electron Devices **2,** 3 (1955).